8-25-2014

Investigation of a mesospheric gravity wave ducting event using coordinated sodium lidar and Mesospheric Temperature Mapper measurements at ALOMAR, Norway (69°N)

Katrina Bossert
University of Colorado Boulder

David C. Fritts
GATS, Inc.

Pierre-Dominique Pautet
Utah State University, dominiquepautet@gmail.com

Michael J. Taylor
Utah State University, mike.taylor@usu.edu

Bifford P. Williams
GATS, Inc.

William R. Pendleton Jr.
Utah State University

AGU PUBLICATIONS

JGR

Journal of Geophysical Research: Atmospheres

RESEARCH ARTICLE
10.1002/2014JD021460

Key Points:
- Lidar and the AMTM provide a new assessment of gravity wave ducting layers
- This technique shows how gravity wave ducts can fluctuate in time and altitude
- Sodium density can be used to validate estimates of ducting calculations

Correspondence to:
K. Bossert,
Katrina.Bossert@gmail.com

Citation:
Bossert, K., D. C. Fritts, P.-D. Pautet, M. J. Taylor, B. P. Williams, and W. R. Pendelton (2014), Investigation of a mesospheric gravity wave ducting event using coordinated sodium lidar and Mesospheric Temperature Mapper measurements at ALOMAR, Norway (69°N), *J. Geophys. Res. Atmos.*, *119*, 9765–9778, doi:10.1002/2014JD021460.

Received 3 JAN 2014
Accepted 5 AUG 2014
Accepted article online 11 AUG 2014
Published online 25 AUG 2014
Corrected 9 OCT 2014

This article was corrected on 9 OCT 2014. See the end of the full text for details.

Investigation of a mesospheric gravity wave ducting event using coordinated sodium lidar and Mesospheric Temperature Mapper measurements at ALOMAR, Norway (69°N)

Katrina Bossert[1,2], David C. Fritts[2], Pierre-Dominique Pautet[3], Michael J. Taylor[3], Bifford P. Williams[2], and William R. Pendelton[3]

[1]Aerospace Engineering Sciences, University of Colorado Boulder, Boulder, Colorado, USA, [2]GATS Inc., Boulder, Colorado, USA, [3]Center for Atmospheric and Space Sciences, Utah State University, Logan, Utah, USA

Abstract New measurements at the ALOMAR observatory in northern Norway (69°N, 16°E) using the Weber sodium lidar and the Advanced Mesospheric Temperature Mapper (AMTM) allow for a comprehensive investigation of a gravity wave (GW) event on 22 and 23 January 2012 and the complex and varying propagation environment in which the GW was observed. These observational techniques provide insight into the altitude ranges over which a GW may be evanescent or propagating and enable a clear distinction in specific cases. Weber sodium lidar measurements provide estimates of background temperature, wind, and stability profiles at altitudes from ~78 to 105 km. Detailed AMTM temperature maps of GWs in the OH emission layer together with lidar measurements quantify estimates of the observed and intrinsic GW parameters centered near 87 km. Lidar measurements of sodium densities also allow more precise identification of GW phase structures extending over a broad altitude range. We find for this particular event that the extent of evanescent regions versus regions allowing GW propagation can vary largely over a period of hours and significantly change the range of altitudes over which a GW can propagate.

1. Introduction

Our understanding of gravity wave (GW) dynamics and their effects in the mesosphere and lower thermosphere (MLT) has advanced dramatically over the last several decades. We now recognize the primary roles of GWs in the MLT to include energy and momentum transport and deposition accompanying GW dissipation, mixing due to turbulence induced by GW instabilities, and various large-scale responses to these small-scale dynamics [e.g., *Holton*, 1982; *Garcia and Solomon*, 1985; *Strobel et al.*, 1985; *Fritts and Alexander*, 2003, and references therein]. Despite these advances, there remain important aspects of GW dynamics and effects that are poorly understood at present, and additional, more quantitative measurements are required to guide modeling and parameterization of these dynamics in global models. In particular, understanding GW contributions to energy and momentum transport, the interaction and instability dynamics that account for GW dissipation and energy and momentum deposition and mixing, and the distinction between GWs that do and do not transport momentum are key needs.

Ground-based instruments have been major contributors to our advancing understanding of GW dynamics in the MLT and elsewhere, and these capabilities continue to improve with time. Radars at frequencies varying from MF to VHF or UHF provide measurements of radial or horizontal winds via backscatter from quasi-tracers of air parcel motions such as refractive index or electron density fluctuations and meteor trails. Fabry-Perot interferometers provide airglow-layer-averaged temperatures and radial winds via measurements of airglow line width and Doppler shift. Rayleigh and resonance lidars enable measurements of densities, temperatures, and/or radial winds inferred from photon counts, Doppler-broadened line widths, and Doppler shifts. Airglow imagers, and the new Mesospheric Temperature Mappers (MTMs), quantify horizontal GW scales, orientations, phase speeds, and spatial extents. MTMs also quantify GW amplitudes to a much greater degree than is possible by airglow imagers alone.

Resonance wind and temperature lidars and airglow imagers have made especially significant contributions to our understanding of GW characteristics, amplitudes, propagation, instabilities, and their influences in the

MLT for several decades. Studies employing individual lidar or airglow instruments cannot quantify GW characteristics as fully as combinations of instruments that define horizontal and vertical GW structures and their environments together. Such studies have nevertheless contributed to our initial understanding of GW scales, periods, phase speeds, likely sources, and propagation directions [e.g., *Taylor and Hapgood*, 1988; *Taylor et al.*, 1993, 1995a, 1997; *Collins et al.*, 1996; *Nakamura et al.*, 1999; *Hu et al.*, 2002; *Bageston et al.*, 2009; *Yue et al.*, 2009].

More comprehensive measurements obtained by combining airglow imaging, lidar, and/or other instruments have characterized GW scales, characteristics, instabilities, and intrinsic properties more completely [e.g., *Swenson et al.*, 1995; *Taylor et al.*, 1995b; *Hecht et al.*, 1997, 2001; *Williams et al.*, 2006; *Isler et al.*, 1997; *Yamada et al.*, 2001; *Li et al.*, 2011]. A number of studies have also addressed the specific dynamics needs noted above. These include estimates of MLT GW momentum fluxes employing various techniques [e.g., *Vincent and Reid*, 1983; *Fritts and Vincent*, 1987; *Reid and Vincent*, 1987; *Reid et al.*, 1988; *Meyer et al.*, 1989; *Tsuda et al.*, 1990; *Wang and Fritts*, 1990; *Hitchman et al.*, 1992; *Murphy and Vincent*, 1993; *Nakamura et al.*, 1993; *Swenson et al.*, 1999; *Gavrilov et al.*, 2000; *Espy et al.*, 2004, 2006; *Suzuki et al.*, 2007; *Antonita et al.*, 2008; *Fritts et al.*, 2010, 2012]. Other studies yielded direct evidence for local instabilities suggesting GW "breaking," dissipation, and energy and momentum deposition [e.g., *Swenson and Mende*, 1994; *Hecht et al.*, 1997; *Yamada et al.*, 2001; *Xu et al.*, 2006; *Li et al.*, 2005, 2007]. Evidence of GW ducting behavior in the MLT has also been obtained [e.g., *Isler et al.*, 1997; *Walterscheid et al.*, 1999; *Simkhada et al.*, 2009], including large-amplitude events now recognized as mesospheric bores [*Taylor et al.*, 1995a; *Dewan et al.*, 1998; *Dewan and Picard*, 2001; *Medeiros et al.*, 2001, 2005; *Smith et al.*, 2003, 2005, 2006; *She et al.*, 2004; *Fechine et al.*, 2005; *Nielsen et al.*, 2006; *Stockwell et al.*, 2006, 2011; *Narayanan et al.*, 2009; *Bageston et al.*, 2011a, 2011b; *Li et al.*, 2013].

Each of these classes of dynamics has proven challenging to quantify fully with MLT measurements that only partially describe the relevant spatial and temporal scales and the relationships between dynamical quantities, especially covariances. Advanced modeling can address all of these dynamics, often for realistic parameters (including viscosity), but often lacks sufficient guidance on initial GW parameters and environmental profiles. Quantification of GW momentum fluxes and their variations accompanying GW filtering, interactions, and instability dynamics is a central need because GWs are the major driver of the mean MLT circulation and thermal structure. However, they are challenging to quantify because they require knowledge of GW amplitudes and velocity covariances, which are difficult to measure directly and are nearly zero for GWs that are ducted rather than freely propagating vertically.

GW instabilities are likewise challenging to identify and quantify because they are inherently nonlinear and multiscale, they display a wide range of possible instability structures, and observations typically lack the precision needed to enable a comprehensive description of GW and environmental parameters [see, e.g., *Lombard and Riley*, 1996; *Sonmor and Klaassen*, 1997; *Fritts and Alexander*, 2003; *Fritts et al.*, 2009a, 2009b, 2013]. Distinguishing between GWs that are vertically propagating and ducting events or mesospheric bores are challenging to characterize with confidence due to various remote and local potential sources and their expected sensitivity and responses to small-scale features in the environmental wind and temperature profiles [*Chimonas and Hines*, 1986; *Fritts and Yuan*, 1989; *Snively and Pasko*, 2003, 2008; *Simkhada et al.*, 2009; *Laughman et al.*, 2009, 2011; *Walterscheid and Hickey*, 2009; *Snively et al.*, 2013].

To address these dynamics observationally in a quantitative manner, we need to define the event characteristics as fully as possible in both the vertical and horizontal directions. Narrowband sodium lidars provide radial wind and temperature measurements at relatively high spatial and temporal resolution. The sodium lidar at the Arctic Lidar Observatory for Middle Atmosphere Research (ALOMAR) typically achieves accuracies of better than 2 m s^{-1} and 1 K for averages over 1.1 km and 1 h. The lidar can further quantify localized vertical gradients of wind and temperature changes with errors better than 0.25 K and 0.4 m s^{-1} for averages over 1 km and 1 h near the peak of the sodium layer. Thus, it is able to quantitatively characterize local horizontal wind and temperature profiles averaged over several GW periods. The new Advanced Mesospheric Temperature Mapper (AMTM) at ALOMAR is likewise able to define GW scales, amplitudes, orientations, phase speeds, and spatial extents to a degree not possible with previous airglow imaging systems.

This paper employs new correlative measurements with the ALOMAR sodium lidar and the AMTM to characterize the ducting environment for small-scale GWs that appear to be confined in altitude near the OH airglow layer observed by the AMTM. This will enable a distinction between GWs that are ducted and those

that are not, hence more accurate GW momentum flux assessments, in future analyses. The sodium lidar and AMTM are described in section 2. Our measurement techniques and analysis are described in section 3. Sections 4 and 5 provide a discussion of the results of our analysis and our conclusions.

2. Instrumentation

This study utilizes complementary measurements from two instruments at ALOMAR, located at 69°N, 16°E and 379 m above sea level. These instruments are the Weber sodium lidar and the AMTM and are described separately below.

2.1. ALOMAR Weber Sodium Lidar

The Weber sodium lidar [*She et al.*, 2002] is a resonance fluorescence lidar that measures winds, temperatures, and sodium densities from about 80 to 105 km. The lidar system uses a sum frequency generator (SFG) to produce about 50 mW of 589 nm light at the sodium D2a resonance line. The frequency is tuned using a sodium vapor cell with Doppler-free saturation spectroscopy [*She and Yu*, 1995]. This light is sent through acousto-optic modulators (AOM) to shift between the center frequency of the D2a line at 589.189 nm and two up and down shifted frequencies at ±630 MHz. These three frequencies allow for the theoretical shape of the D2a line to be calculated, providing radial wind and temperature estimates [*She et al.*, 2002; *She and Yu*, 1994]. When the lidar beams are tilted off zenith, zonal and meridional components of the wind field can be obtained by suitable averaging in time.

The CW light from the SFG and AOMs is sent through a pulsed dye amplifier (PDA) pumped with a Spectra-Physics 50 Hz neodymium: yttrium/aluminum/garnet laser. The emitted PDA pulses have a full-width-half maximum (FWHM) duration of 6.7 ns and a FWHM linewidth of 130 MHz. The emitted power is about 400 mW. The outgoing beam is expanded to a size of 20 mm with a divergence of 0.5 mrad. This leads to a sampling area size of about 40 m in diameter at 80 km when the beam is pointed at zenith.

The return photons are collected using two 1.8 m diameter IAP telescopes. These telescopes can be steered up to 30° off zenith. For the data set described in this paper, data were taken at 20° off zenith. The returns are counted using Hamamatsu photomultipliers. A 50 Hz chopper removes low-altitude returns to prevent saturation. The range bin size for a beam configured at zenith is 150 m. The system shifts between each of the three frequencies and remains for 5 s at each frequency, allowing for a minimum integration time of 15 s.

2.2. Advanced Mesospheric Temperature Mapper

The Utah State University (USU) AMTM provides 2-D spatial and temporal measurements of the mesospheric OH(3,1) band rotational temperatures and OH intensity perturbations over a nominal field of view of 144 km by 180 km centered on the zenith. These temperatures are a weighted average over the nocturnal OH layer, which is generally centered near 87 km with a FWHM of ~8 km [*She and Lowe*, 1998; *von Zahn and Fricke*, 1987; *Baker and Stair*, 1988].

The AMTM uses a fast (f:1) 120° field-of-view telecentric lens system designed and built at the USU Space Dynamics Laboratory. Three 4 in narrowband (2.5–3 nm) filters mounted in a temperature-stabilized filter wheel are used to sequentially measure the OH (3,1) P_{12} and P_{14} lines, as well as a nearby background sky emission. The data are then imaged using an infrared InGaAs (320 × 256 pixel) detector thermoelectrically cooled to −50°C to limit the electronic noise, and controlled through a USB port by a Windows computer. At ALOMAR the exposure time for each filter is typically 10 s, giving a temperature measurement for each of the 81,920 pixels every ~30 s. This imager can acquire data under full Moon conditions with only limited reduction in GW detection and measurement capabilities. The AMTM is a relatively new instrument development, and two have been built to date. The first one has operated at the South Pole Station (90°S) since 2010, and the second one has operated at ALOMAR since the winter 2010–2011. During the summer months, the ALOMAR AMTM is returned to USU and runs on campus (42°N) alongside the USU sodium lidar. The AMTM OH rotational temperature data have been cross calibrated using concurrent Na lidar measurements yielding a temperature precision of ~1 K (in 30 s) and an accuracy of ±5 K with respect to height-weighted lidar measurements centered at the nominal OH emission altitude of 87 km.

3. Measurement Techniques and Analysis

The measurement techniques described in this section allow for a vertical and temporal characterization of the GW propagation environment. This yields quantitative information about whether the observed

GWsare freely propagating, potentially ducted within the observed altitude range, or evanescent at all observed altitudes.

The AMTM provides spatial temperature measurements in time from which GW horizontal phase speed and wavelength estimates can be obtained for GW motions yielding coherent responses across the OH layer. A better approximation for the mean altitude of the AMTM OH measurements is determined through an iterative process by correlating AMTM measurements with sodium lidar data using different weighting scales and altitudes [*Melo et al.*, 2001; *Zhao et al.*, 2005].

In conjunction with the AMTM, the Weber sodium lidar provides radial wind, temperature, and density measurements averaged in time at a specific location from ~80 to 105 km. The sodium number density is calculated using the theoretical sodium backscatter cross section and Rayleigh normalization [*Fricke and von Zahn*, 1985]. Rayleigh normalization uses counts fitted from 29 to 35 km with Mass Spectrometer Incoherent Scatter values for predicted normalized densities at the Rayleigh measurement altitudes. The temperatures, winds, and corresponding uncertainties were calculated using ratios of the return frequency counts [*Papen et al.*, 1995].

3.1. Gravity Wave Environment Calculations

Conditions for freely propagating or ducting GWs are calculated using measured GW parameters from the lidar and AMTM. To determine the propagation characteristics of observed GWs, the buoyancy frequency and the vertical wave number must be calculated. The squared buoyancy frequency is calculated using the relation

$$N^2 = \frac{g}{T}\left(\frac{\mathrm{d}T}{\mathrm{d}z} + \Gamma\right) \tag{1}$$

where T is the average temperature obtained with the sodium lidar, $\mathrm{d}T/\mathrm{d}z$ is the temperature gradient, $g = 9.54\ \mathrm{m\ s^{-1}}$ is the gravitational acceleration, and $\Gamma = 9.5\ \mathrm{K\ km^{-1}}$ is the appropriate adiabatic lapse rate.

The vertical wave number, m, allows for a distinction to be made between GWs that are freely propagating in the vertical ($m^2 > 0$), GWs that are evanescent at all observed altitudes ($m^2 < 0$), or gravity waves that are trapped or ducted in a region where $m^2 > 0$ but bounded by regions having $m^2 < 0$ [*Isler et al.*, 1997]. The vertical wave number squared can be estimated from the dispersion relation neglecting wind shear and curvature terms [see *Fritts and Alexander*, 2003]. However, in regions having variable horizontal winds, it is often important to account for these influences [*Simkhada et al.*, 2009]. This more complete version of the dispersion relation may be written as [*Nappo*, 2013]

$$m^2 = \frac{N^2}{(c-u)^2} + \frac{1}{(c-u)}\frac{\mathrm{d}^2u}{\mathrm{d}z^2} - \frac{1}{H(c-u)}\frac{\mathrm{d}u}{\mathrm{d}z} - \frac{1}{4H^2} - k^2 \tag{2}$$

Here H is the scale height, N is the buoyancy frequency, and k, c, and u are the GW horizontal wave number, the GW horizontal phase speed, and the background wind speed in the plane of GW propagation. N and u are measured from the lidar, and k and c are obtained from the AMTM.

3.2. Sodium Density Perturbation Calculations

As a further means to describe GW responses to their propagation environments, perturbations in the sodium density are used to track vertical displacements more accurately than can be inferred from lidar and AMTM wind and temperature measurements. Sodium density perturbations due to GWs have previously been simulated [*Swenson and Gardener*, 1998; *Shelton et al.*, 1980] using a relation derived by *Chiu and Ching* [1978]. Sodium density perturbations can be derived from the sodium continuity equation and are given by

$$\rho_s' e^{-i\omega t} = \left[\left(\frac{w'}{i\hat{\omega}}\right)\left[\frac{\overline{\rho}_s}{H} + \frac{\partial\overline{\rho}_s}{\partial z}\right] + \overline{\rho}_s\frac{\rho'}{\overline{\rho}}\right]e^{-i\omega t} \tag{3}$$

Here ρ_s' is the sodium density perturbation, $\overline{\rho}_s$ is the mean sodium density at each altitude, $\overline{\rho}$ is the mean density at each altitude, ρ' is the atmospheric density perturbation at each altitude, $\hat{\omega} = \omega - ku$ is the intrinsic frequency, and ω is the relative frequency as observed by a ground-based observer.

Lidar temperature measurements do not achieve the small uncertainties required to define temperature and vertical wind perturbations associated with small-amplitude, short-period GWs with high confidence. However, the AMTM provides high-precision temperatures averaged over the OH layer near 87 km at high horizontal and temporal resolution. These temperatures provide accurate estimates of the temperature perturbations for GWs having sufficiently large vertical wavelengths to avoid significant phase cancelation across the OH airglow layer depth [*Snively et al.*, 2009].

Equation (3) can be rewritten in terms of the temperature perturbations measured from the AMTM by using the Boussinesq polarization relations to relate wind, temperature, and density perturbations. This relation is given by where T' is the temperature perturbation and $\overline{T}$ is the local average background temperature.

$$\rho_s' e^{-i\omega t} = \left[\left(\frac{g}{N^2}\frac{T'}{\overline{T}}\right)\left[\frac{\overline{\rho}_s}{H} + \frac{\partial\overline{\rho}_s}{\partial z}\right] + \overline{\rho}_s\frac{T'}{\overline{T}}\right]e^{-i\omega t} \tag{4}$$

where T' is the temperature perturbation and $\overline{T}$ is the local mean background temperature.

The AMTM only provides temperature measurements at the OH layer. However, by assuming a propagating GW, the temperature can be predicted at all altitudes. Additionally, GW momentum flux must be constant with altitude for a steady nondissipating, vertically propagating GW, which gives the following relation:

$$\rho(z)u'(z)w'(z) = \rho(z_o)u'(z_o)w'(z_o) \tag{5}$$

The background density in equation (5) varies with altitude as

$$\rho(z) = \rho_o e^{-z/H} \tag{6}$$

Using equations (5) and (6) and assuming a propagating GW and stable environment (e.g., $N^2 > 0$ and $\hat{\omega} < N$), a relation between the temperature perturbation measured by the AMTM and temperature perturbations at other altitudes can be obtained. This relation is given by

$$\frac{T'(z)}{\overline{T}(z)} = e^{(z-z_o)/(2H)}\sqrt{\frac{N^3(z)}{N_o^3(z_o)}}\frac{T'(z_o)}{\overline{T}(z_o)} \tag{7}$$

Equation (7) yields a vertical profile of T', or ρ_s' from equation (4), for GWs satisfying the above assumptions. Altitudes at which a GW has a vertically propagating character should yield close agreement with the predicted altitude variations in T' and ρ_s'. However, altitudes at which the predicted sodium density perturbations do not closely resemble the measured sodium density perturbations imply a region where the GW structure in the vertical *does not* conform to the above assumption. In this way, the measured sodium density profiles can allow us to distinguish between GWs that are vertically propagating and those that may be evanescent or ducted at specific altitudes.

3.3. Error Calculations

As both N^2 and m^2 depend on measured quantities with inherent uncertainties, we have employed an error propagation analysis to assess the expected uncertainties in the N^2 and m^2 profiles. Averaging was employed for the various fields to achieve a reasonable compromise between error and precision of our estimates. The error for N^2 is given by

$$\Delta N^2 = N^2\sqrt{\left(\frac{1}{\frac{(T_2-T_1)}{(z_2-z_1)}+\Gamma}\right)^2\left(\frac{\sqrt{2}\Delta T}{(z_2-z_1)}\right)^2 + \left(\frac{\Delta T}{\overline{T}}\right)^2} \tag{8}$$

The error calculation for m^2 is dependent on uncertainties arising from measurements of the GW horizontal phase speed and horizontal wavelength, errors in the calculated buoyancy frequency given by equation (8), and the wind shear and curvature terms. A general equation for the m^2 error calculation may be written as

$$\Delta m^2 = \sqrt{\left(\frac{\partial m^2}{\partial N^2}(\Delta N^2)\right)^2 + \left(\frac{\partial m^2}{\partial \hat{c}}(\Delta \hat{c})\right)^2 + \left(\frac{\partial m^2}{\partial k^2}(\Delta k^2)\right)^2 + \left(\frac{\partial m^2}{\partial u_z}(\Delta u_z)\right)^2 + \left(\frac{\partial m^2}{\partial u_{zz}}(\Delta u_{zz})\right)^2} \tag{9}$$

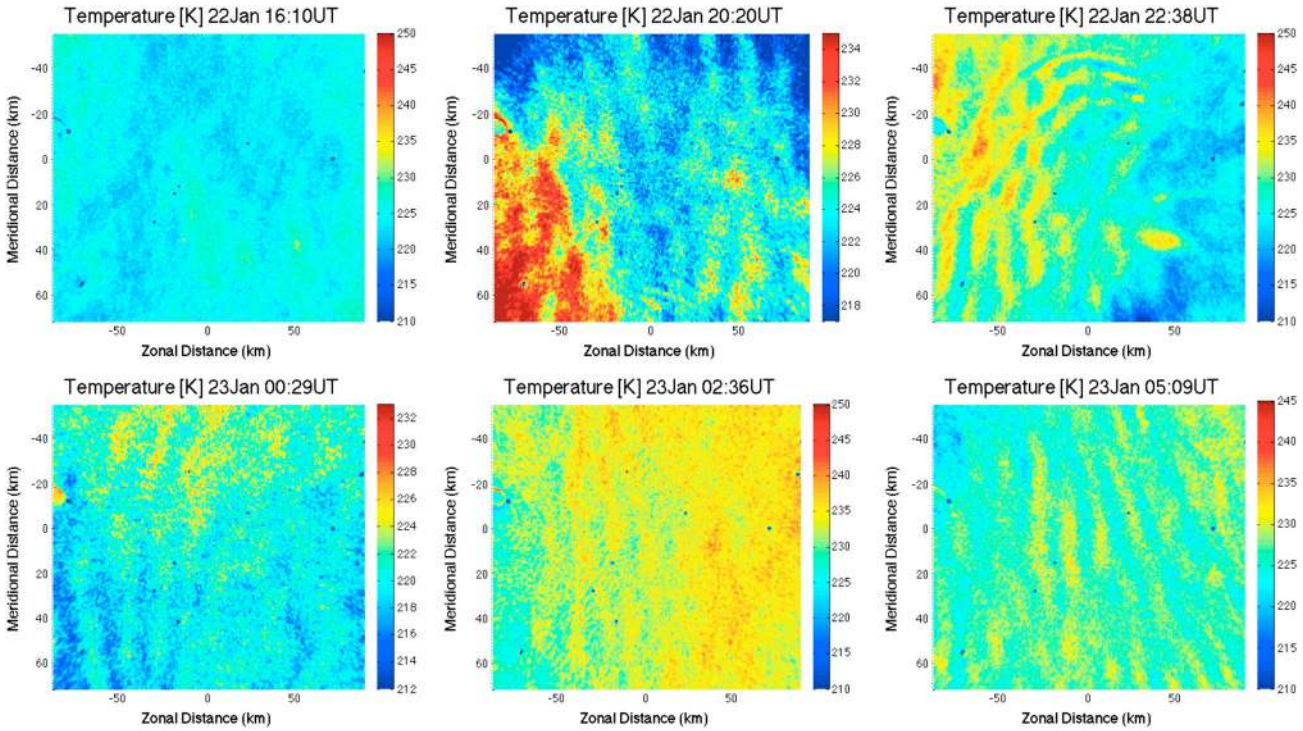

Figure 1. AMTM spatial temperature maps show observed waves throughout the night of 22–23 January 2012 starting shortly after 20 UT. Times are shown at the top of each panel. North and East are up and to the right. Note the differing temperature scales in each panel.

where $\hat{c}$ denotes the GW intrinsic phase speed, u_z denotes wind shear, and u_{zz} denotes wind curvature. The full error calculation for m^2 as calculated from equation (9) is given by

$$\Delta m^2 = \sqrt{\left[\left(\frac{1}{\hat{c}^2}\right)(\Delta N^2)\right]^2 + \left[\left(\frac{-2N^2}{\hat{c}^3} - \frac{u_{zz}}{\hat{c}^2} - \frac{u_z}{H\hat{c}^2}\right)(\Delta \hat{c})\right]^2 + \left[\frac{8\pi}{\lambda^3}(\Delta\lambda)\right]^2 + \left[\left(\frac{1}{H\hat{c}}\right)\left(\frac{\sqrt{2}}{dz}\Delta u\right)\right]^2 + \left[\left(\frac{1}{\hat{c}}\right)\left(\frac{2\Delta u}{(dz)^2}\right)\right]^2} \quad (10)$$

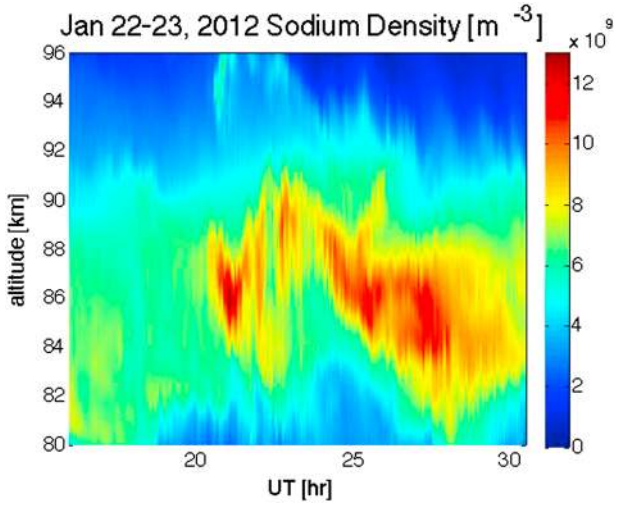

Figure 2. Sodium densities measured with the sodium resonance lidar at ALOMAR using a 1 min integration and 150 m range resolution on 22–23 January 2012.

4. Results and Discussion

On 22 and 23 January 2012, a long-lived (>9.5 h) short-period ($T < 15$ min) GW event was observed throughout the night using our collocated instruments at ALOMAR. The GW was apparent during several time intervals in the AMTM from around 19:00 UT on 22 January to 5:30 UT on 23 January. Figure 1 shows several AMTM images of the GW structure throughout the night. The GW appeared to be propagating almost entirely from the east to the west. For a short period during the night, a second GW was also observed (an example of this is shown in the figure at 22:38 UT). However, these results will focus on the primary GW that was observed for the majority of the night moving from east to west.

Using successive AMTM images, the average horizontal phase speed of the GW

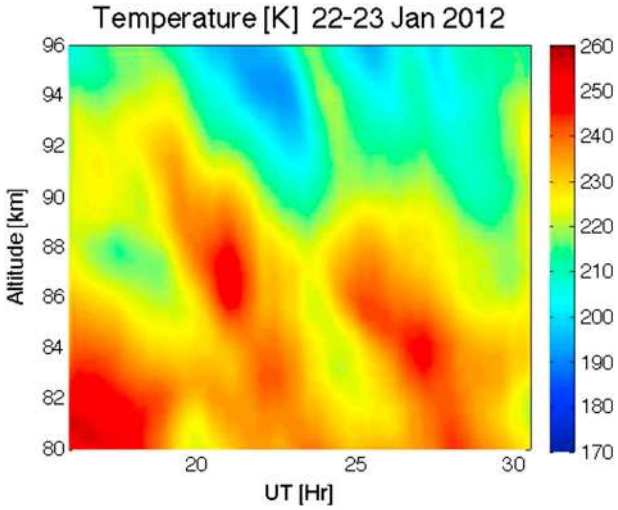

Figure 3. Temperature profiles measured with the sodium lidar using 1.128 km and 1 h averaging on 22–23 January 2012.

was measured at several times throughout the observation interval and was determined to be ~34.5 m s^{-1} ± 3.4 m s^{-1} to the west. The mean wavelength of the GW was 18.9 km ± 1.5 km. These estimates result in observed GW periods of $T_{obs} = \lambda/c = 9.1 \pm 1.5$ min. The temperature perturbation for this GW was estimated from multiple AMTM images throughout the night by evaluating the temperature amplitude of the GW using cross sections from the AMTM images. For this night, the average temperature perturbation was found to be 2.5 K ± 0.6 K.

Sodium densities were calculated using an integration time of 1 min and are shown throughout the night in Figure 2. The calculated error for the 1 min sodium densities between 79 km and 96 km is ~10^8 m^{-3}. Measured sodium density perturbations were observed with amplitudes on the order of ~1×10^9 m^{-3}, which is several times the calculated error for this integration. Winds and temperatures were calculated averaging two lidar beams using 1 h averaging with a 10 min sliding window and vertical averaging of 1.128 km with a 0.141 km sliding windows. The resulting average errors for the 1.128 km and 1 h averaged temperature and wind based on photon noise between 79 km and 96 km are 0.19 K and 0.32 m s^{-1}. These errors calculated from photon noise are used in the error calculations for N^2 and m^2. Estimated temperatures and horizontal winds in the westward direction of observed GW propagation for the night are shown in Figures 3 and 4.

Temporal and vertical estimates of N^2 are shown in Figure 5. A value of $N^2 < 0$ implies a statically unstable atmosphere. On this night, the atmosphere was found to be relatively stable. However, there are several regions of small N^2 that can possibly lead to an unfavorable propagation environment for the GW when the buoyancy period is larger than the intrinsic GW period. The median percentage error for N^2 between 79 km and 96 km was found to be 2.9% using the 1 h and 1.128 km averaging from both lidar beams. A plot of the errors associated with the N^2 calculation is shown in Figure 6. Using these N^2 values, calculations for m^2 were made.

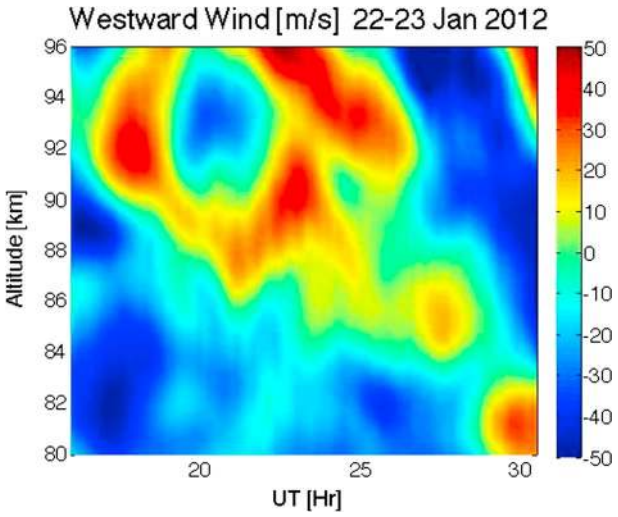

Figure 4. As in Figure 3 but for winds in the direction of GW propagation from east to west. Radial winds were converted to horizontal winds assuming vertical winds are zero for a 1 h average.

The m^2 values were calculated to correspond to a GW with a horizontal wavelength $\lambda = 18.9$ km and a phase speed $c = 34.5$ m/s toward the west, so that an average of the observed parameters could be provided. These m^2 values were calculated using equation (2). The resulting m^2 values are given in Figure 7. The errors for these m^2 values were calculated using equation (10) and a plot of these errors is given in Figure 8. The median percent error associated with m^2 between 79 km and 96 km is 47.3%.

Estimates of ρ_s' were obtained using calculated values for N^2, the GW temperature perturbation estimates from the AMTM, and the vertical sodium density gradient obtained from a 20 min smoothed sodium density profile. The OH layer peak

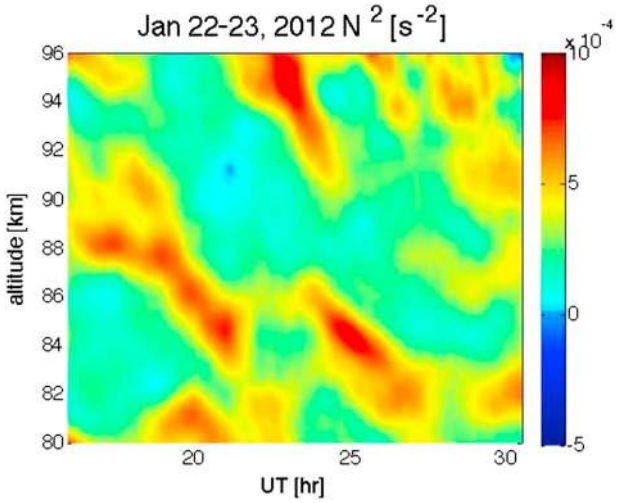

Figure 5. N^2 calculated using the temperatures shown in Figure 3.

was found to be at 86 km with a FWHM of 8 km, so measured temperature perturbations from the AMTM are assumed to correspond to this center altitude. Predicted ρ_s' are calculated by conforming to the relation given by equation (5) and assuming that the GW is propagating in a stable environment at all altitudes and times. Additionally, phases imposed on the predicted density perturbations are relative and assumed to be zero in altitude over a range of a few kilometers (as if the vertical wavelength is very large, for convenience). Assuming a specific smaller vertical wavelength and corresponding phase variation with altitude would also be possible, but it would not alter the pattern of time-height variations of ρ_s' we intend to compare with observations. The period for the density perturbation is calculated using observed phase speeds from the AMTM.

We expect phase changes in ρ_s' in altitude that vary depending on m^2 where a GW is propagating [*Vadas and Nicolls*, 2009]. However, these are necessarily small for vertical wavelengths larger than the vertical extent of reliable lidar ρ_s' measurements, typically spanning $<$20 km. As noted, though, this analysis emphasizes comparisons of the amplitudes of predicted versus measured ρ_s' to interpret where GWs have propagating versus evanescent behavior.

Plots for the predicted and measured ρ_s' for three different periods during the GW event throughout this night are shown in Figure 9 together with the corresponding calculated m^2 values. The left plots in Figure 9 show the predicted ρ_s' calculated from equation (4) using the smoothed background density, N^2 values, and measured GW parameters measured by the AMTM. The predicted ρ_s' was calculated using the average measured GW parameters and temperature perturbations for the entire the night. The center plots show the measured ρ_s'. These are obtained by subtracting the smoothed sodium density profile from the raw density profile. The right plots show the zoomed views of the corresponding m^2 values calculated from lidar winds and temperatures and AMTM GW parameters that were previously shown for the entire night in Figure 7. In these three cases, regions of good agreement between the amplitude of the predicted and measured ρ_s' indicate the GW is either propagating with similar characteristics to the GW observed from the AMTM or distributed across ducting regions. Regions where there is poor matching between the amplitudes of predicted and measured ρ_s' indicate that the GW is likely not propagating in that region. For example, if the perturbation amplitudes are smaller at an altitude above the OH layer, it could indicate that the wave has decayed or is evanescent in that region. These areas of similar or differing predicted versus measured ρ_s' amplitudes can be compared to calculated m^2 values which show regions of $m^2 > 0$ or $m^2 < 0$ indicating more likely altitudes for propagating or evanescent responses. In this way, assessments of locations of GW propagation in time and altitude can be made.

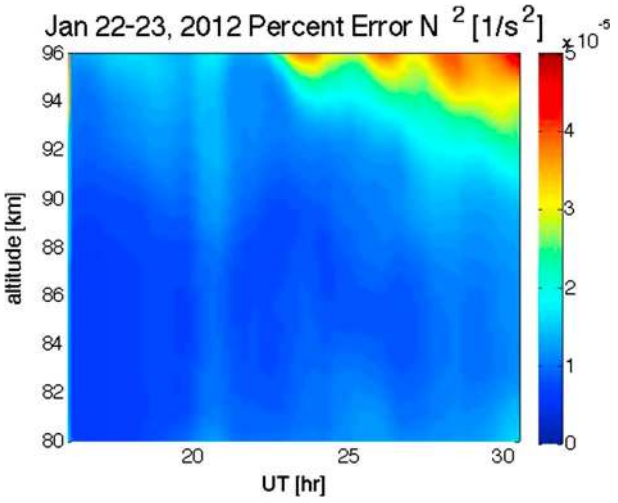

Figure 6. Errors calculations from equation (8) associated with N^2 calculated from equation (1).

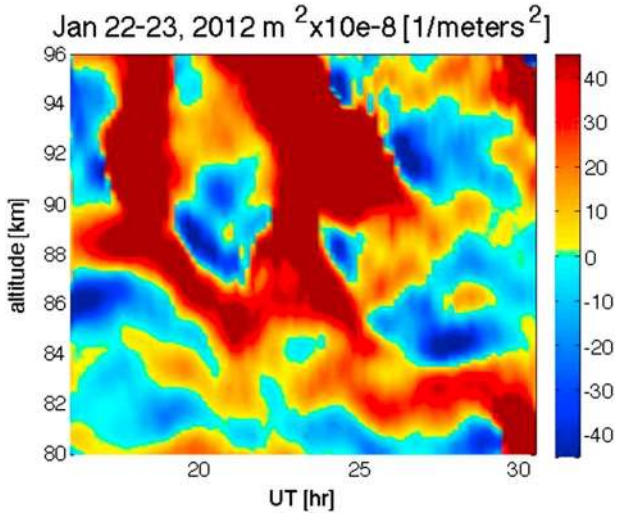

Figure 7. Values of m^2 calculated including the wind shear and curvature terms.

Figures 9a–9c show predicted and measured ρ_s' and m^2 from 16 UT to 22 UT. Figure 9a shows the predicted ρ_s' for an assumed propagating GW with a temperature perturbation of 2.5 K at 86 km. It should be noted that temperature perturbations were first observed in the AMTM just before 19 UT. However, a GW with a temperature perturbation of 2.5 K was imposed on the background sodium density field for the entire interval. In the simulated ρ_s' shown in Figure 9a, if a GW were to be propagating between the times of 16 UT and 18 UT with a T' amplitude of 2.5 K at 86 km, ρ_s' would be easily observable near 80 km and still moderately observable from 82 km to 88 km. Conversely, the measured ρ_s' in Figure 9b shows measured ρ_s' that are smaller in amplitude at 80 km than the predicted and measured ρ_s' that are largely unobservable above this point. This implies that a GW may have been present at lower altitudes but did not yield significant displacements extending to higher altitudes. During this period, the AMTM did not observe any GWs, which also suggests that the GW observed in the sodium layer near 80 km did not extend to altitudes near the OH layer peak. The m^2 fields displayed in Figure 9c show that the atmospheric conditions lead to a largely evanescent region between 81 and 87 km for this particular GW, including a very strongly evanescent region near 86 km. Given that this evanescent region is large in vertical extent, and the ρ_s' observed at 80 km are much smaller than those predicted for a T' of 2.5 K, it seems likely that the GW observed in the measured ρ_s' was ducted at a lower altitude and had decayed in amplitude to the point where it could no longer be observed in the AMTM at 86 km due to evanescence.

Continuing with this interval, measured ρ_s' were observable near 82 km from 19 UT to later times. However, the background sodium density had a nearly constant mixing ratio at somewhat higher altitudes, so that if a GW were to be propagating, it would not be observable in the sodium density layer above 82 km at 19 UT. The AMTM observed a GW starting slightly before 19 UT, which indicates that the GW associated with the ρ_s' at 82 km and 19 UT may also be present with measurable amplitudes at higher altitudes. One reason this GW began to be observable in the AMTM around 19 UT is that a region having $m^2 > 0$ appeared after this time from 82 to 84 km where the environment had been largely evanescent before. This region appears to have allowed the GW to reach higher altitudes than before by tunneling between regions having $m^2 > 0$. Somewhat after 20 UT, the characteristics of the background sodium density layer allowed for observable GW ρ_s', and these perturbations clearly revealed the GW to extend to 86 km near the peak of the OH layer, which is also a region of $m^2 > 0$ according to Figure 9c. The analysis of this interval provides evidence that while large regions of evanescence in altitude can prevent a GW from reaching

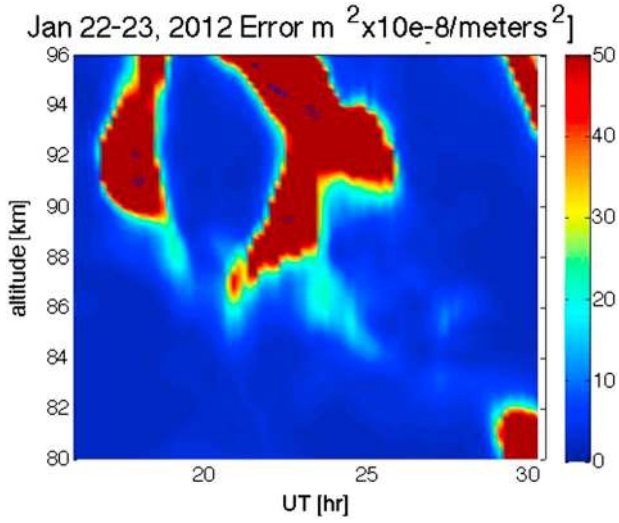

Figure 8. Error calculated from equation (10) associated with m^2 calculation using equation (2).

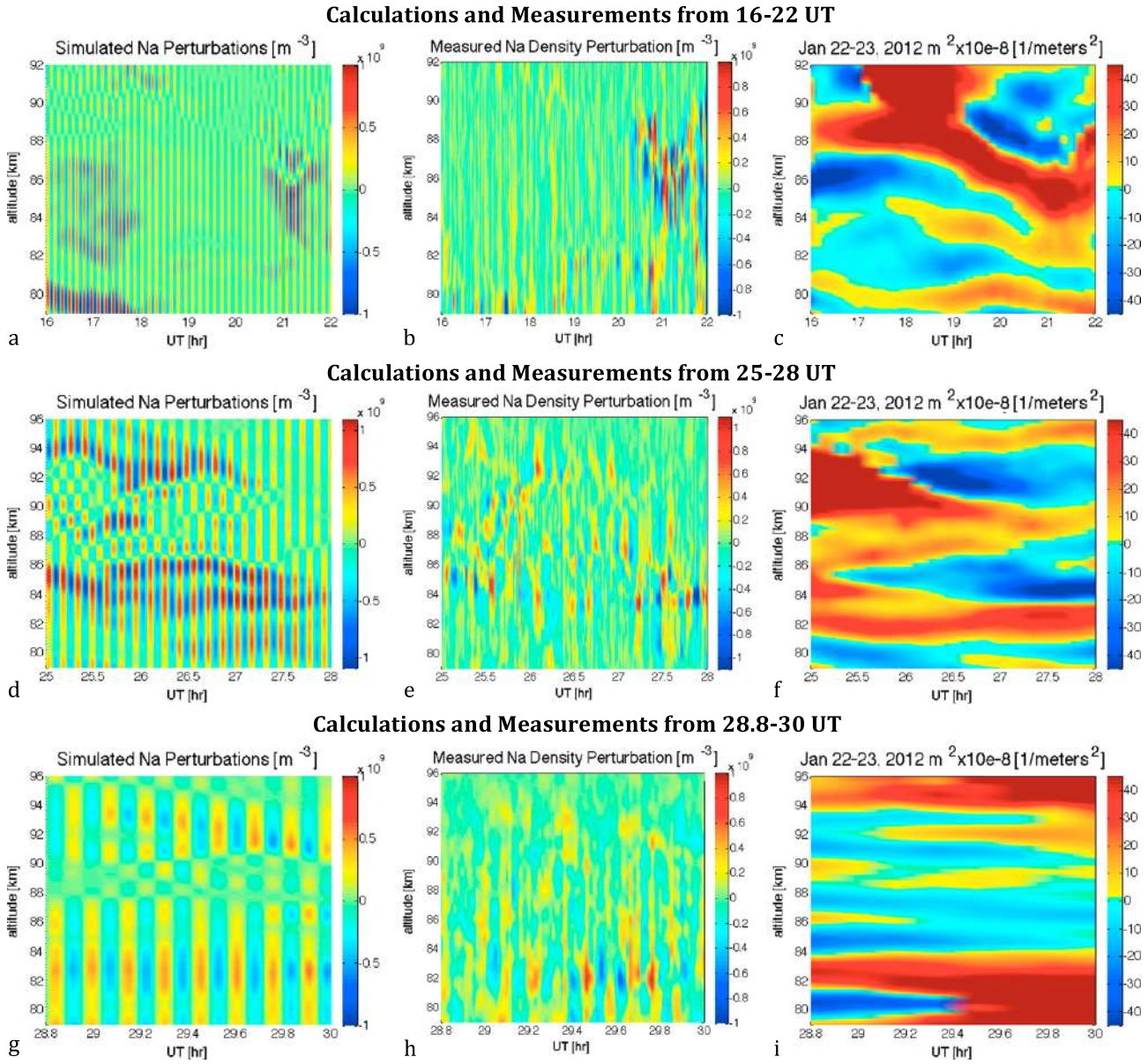

Figure 9. (a, d, and g) Predicted density perturbations using a constant temperature perturbation in altitude and time, the smoothed background sodium density, and average GW parameters measured over the night. (b, e, and h) Measured sodium density perturbations. (c, f, and i) Values of m^2 for the corresponding time and altitude intervals. (left to right) Time intervals from 23.5 to 26.5 UT, 20 to 23 UT, and 28 to 06 UT. Calculations were made using an average of GW parameters observed throughout the night.

higheraltitudes, alternating regions of evanescence and vertical propagation over a few kilometers in altitude can allow a ducted GW to achieve a much larger vertical extent.

Figures 9d–9f show times from 25 to 28 h (1–4 UT on 23 January 2012). During this time it appears that the predicted ρ_s' in Figure 9d overestimates the measured ρ_s' near 86 km. Additionally, the measured ρ_s' shown in Figure 9e decrease as altitude increases. This is especially apparent near 94 km where the predicted ρ_s' are strong, but the measured ρ_s' are very weak. Figure 9f exhibits a strong evanescent region starting near 25 h and 90 km. It is possible at this time that a GW was propagating at a lower altitude but failed to penetrate multiple evanescent regions at higher altitudes, which would cause a much lower measured ρ_s' above 94 km. The comparison between the measured and predicted ρ_s' suggests that the GW observed in the AMTM may have been intermittently propagating and evanescent at the OH layer at these times due to multiple evanescent regions below 87 km.

Figures 9g–9i show data from the end of the night when the GW was still visible in the AMTM data. In Figure 9g, ρ_s' predictions show small-amplitude perturbations throughout the layer that can be seen clearly at 94 km. However, the measured ρ_s' in Figure 9h are only easily apparent near 82 km and quite faint above this region. Investigation of the m^2 values in Figure 9i shows a mostly evanescent region from 84 to 94 km. Additionally, a region of large $m^2 > 0$ is seen below 84 km. Given the altitude of the most easily observed ρ_s', it seems likely that the GW is ducted below 84 km and evanescent above this region. The GW T' measurements from the AMTM are averaged over regions having larger and smaller dT'/dz, which results in an underestimate of T' when significant variations in dT'/dz are within the airglow layer. This accounts for the stronger than predicted measured ρ_s' at 82 km and weaker than predicted measured ρ_s' at higher altitudes where the wave may be evanescent for the assumed GW T' based on the AMTM estimate.

Each of the three cases described above shows evidence of a GW that may have been propagating at lower altitudes, or in the lower altitude range of the sodium density profile, and was likely evanescent at several altitudes throughout the sodium density layer from 79 km to 96 km. The conditions varied throughout the night in the three cases, and at various times the evanescent regions extended over a large depth, preventing the GW from reaching higher altitudes. All three cases showed evidence of a GW that was ducted or confined at some altitude given the evanescent regions in the m^2 profile.

These measurements utilizing the sodium lidar are only available over a range of ~20 km, so it is difficult to predict the origin of the observed waves. The observed GW or GWs could be propagating from a nearby region, or these GWs could have been ducting over a significant horizontal range. Given the complexity of the region observed from 79 km to 96 km, it is possible that the GW could be propagating through multiple ducting regions. It is interesting that this GW, or multiple similar characteristic GWs, persisted throughout most of the night despite the changing atmospheric conditions. During all times of the night, there were observable evanescent regions in addition to regions of $m^2 > 0$ (ducts), which gives evidence that ducting regions may provide stable enough environments for GWs to propagate for extended periods of time.

The results discussed above suggest that this measurement and analysis technique employing measured and computed ρ_s' enables more quantitative characterization of GW propagation environments than without such a comparison. In particular, it provides a method for distinguishing evanescent GWs from propagating GWs in complex and temporally evolving environments. Specifically, comparisons of m^2 values and sodium density perturbations permit assessments of the altitudes at which observed GWs exhibit evanescent or ducted behaviors as opposed to propagating vertically.

5. Conclusions

We have developed a new method of characterizing GW propagation environments that employs measured and estimated sodium density perturbations, ρ_s', to assess GW amplitude variations in altitude more completely than can be inferred from wind and temperature measurements alone. The method was demonstrated using data from 22 to 23 January 2012 to characterize GWs observed by the AMTM and sodium lidar at ALOMAR. Vertical and temporal averaging of lidar and AMTM data enabled calculations of the squared vertical wave number, m^2, for specific GW parameters. This allowed a prediction of GW propagation characteristics, specifically predictions of altitudes at which the GWs may be freely propagating, ducted, or evanescent. The data collected on this occasion yielded insights into the complexity of GW propagation environments for shorter period GWs and showed that rapidly changing environments in altitude between regions yielding evanescent or propagating behavior readily change the extent in altitude over which a GW is observed. The data show that the GWs observed throughout the night were likely ducted at lower altitudes and possibly tunneled between several regions of expected ducting behavior. Similar short-period GW events have been observed by the AMTM on a number of other occasions, suggesting that ducting of short-period GWs in the MLT region may be common at high latitudes.

The accuracy of this method is dependent on the uncertainty associated with measurements of GW and mean profiles of wind, temperature, and sodium density. Temperature and wind measurements must be properly averaged to ensure accurate estimates of these mean profiles. In this study, averages of 1 h and 1.128 km result in uncertainties of an acceptable fraction of typical measured values. Accurate mean profiles

enable estimates of sodium density perturbations that allow comparisons of measurements and assumed distributions for various environments and evaluations of the accuracy of the assumed GW behavior.

Calculated and measured ρ_s' suggest that calculated values of N^2, m^2, and AMTM temperatures provide valuable insights into GW propagation behavior. Utilization of the Na density measurements thus provides another layer of validation to these measurements for studies of small-scale GW structure and behavior.

This study has also revealed that the ducting environment can vary significantly in time while continuing to support GWs having similar character as the ducting environment evolves. Dual lidar and AMTM measurements also allow more spatially precise predictions of ducting given their combined sensitivity to both horizontal and vertical variations of the GW and mean fields. We expect that applications of these methods will also be of value at other sites benefiting from correlative lidar and MTM measurements.

Acknowledgments

The Weber sodium lidar research at ALOMAR was supported by the National Science Foundation under grants AGS-1136269 and AGS-1259136. The lidar was originally developed and installed at ALOMAR with AFOSR DURIP funding to C.-Y. She at CSU. The design and initial development of the AMTM was supported under a separate AFOSR DURIP grant to M. Taylor at the USU Research Foundation, and we gratefully acknowledge R. Esplin and D. Mclain for their expertise and help in its development and testing. The AMTM installation and current operations at ALOMAR are supported under an NSF collaborative grant AGS-1042227. We also acknowledge facility support by the Institute of Atmospheric Physics in Germany.

References

Antonita, T. M., G. Ramkumar, K. K. Kumar, and V. Deepa (2008), Meteor wind radar observations of gravity wave momentum fluxes and their forcing toward the Mesospheric Semiannual Oscillation, *J. Geophys. Res.*, *113*, D10115, doi:10.1029/2007JD009089.

Bageston, J. V., C. M. Wrasse, D. Gobbi, H. Takahashi, and P. B. Souza (2009), Observation of mesospheric gravity waves at Comandante Ferraz Antarctica Station (62°S), *Ann. Geophys.*, *27*, 2593–2598. [Available at www.ann-geophys.net/27/2593/2009.]

Bageston, J. V., C. M. Wrasse, P. P. Batista, R. E. Hibbins, D. C. Fritts, D. Gobbi, and V. F. Andrioli (2011a), Observation of a mesospheric front in a thermal-doppler duct over King George Island, Antarctica, *Atmos. Chem. Phys.*, *11*, 12,137–12,147, doi:10.5194/acp-11-12137-2011.

Bageston, J. V., C. M. Wrasse, R. E. Hibbins, P. P. Batista, D. Gobbi, H. Takahashi, D. C. Fritts, V. F. Andrioli, J. Fechine, and C. M. Denardini (2011b), Case study of a mesospheric wall event over Ferraz station, Antarctica (62°S), *Ann. Geophys.*, *29*, 209–219, doi:10.5194/angeo-29-209-2011.

Baker, D. B., and A. T. Stair (1988), Rocket measurements of the altitude distributions of the Hydroxyl Airglox*, *Phys. Scr.*, *37*, 611–622.

Chimonas, G., and C. O. Hines (1986), Doppler ducting of atmospheric gravity-waves, *J. Geophys. Res.*, *91*, 1219–1230, doi:10.1029/JD091iD01p01219.

Chiu, Y. T., and B. K. Ching (1978), The response of atmospheric and lower ionospheric layer structures to gravity waves, *Geophys. Res. Lett.*, *5*(6), 539–542, doi:10.1029/GL005i006p00539.

Collins, R. L., X. Tao, and C. S. Gardener (1996), Gravity wave activity in the upper mesosphere over Urbana, Illinois: Lidar observations and analysis of gravity wave propagation models, *J. Atmos. Sol. Terr. Phys.*, *58*(16), 1905–1926.

Dewan, E. M., and R. H. Picard (2001), On the origin of mesospheric bores, *J. Geophys. Res.*, *106*(D3), 2921–2927, doi:10.1029/2000JD900697.

Dewan, E. M., R. H. Picard, R. R. O'Neil, H. A. Gardiner, J. Gibson, J. D. Mill, E. Richards, M. Kendra, and W. O. Gallery (1998), MSX satellite observations of thunderstorm-generated gravity waves in mid-wave infrared images of the upper stratosphere, *Geophys. Res. Lett.*, *25*, 939–942, doi:10.1029/98GL00640.

Espy, P. J., G. O. L. Jones, G. R. Swenson, and M. J. Taylor (2004), Tidal modulation of the gravity-wave momentum flux in the Antarctic mesosphere, *Geophys. Res. Lett.*, *31*, L11111, doi:10.1029/2004GL019624.

Espy, P. J., R. E. Hibbins, G. R. Swenson, J. Tang, M. J. Taylor, D. M. Riggin, and D. C. Fritts (2006), Regional variations of mesospheric gravity-wave momentum flux of Antarctica, *Ann. Geophys.*, *24*, 81–88.

Fechine, J., A. F. Medeiros, R. A. Buriti, H. Takahashi, and D. Gobbi (2005), Mesospheric bore events in the equatorial middle atmosphere, *J. Atmos. Sol. Terr. Phys.*, *67*(17–18), 1774–1778.

Fricke, K. H., and U. von Zahn (1985), Mesopause temperatures derived from probing the hyperfine structure of the D2 resonance line of sodium by lidar, *J. Atmos. Sol. Terr. Phys.*, *47*(5), 499–512.

Fritts, D. C., and M. J. Alexander (2003), Gravity wave dynamics and effects in the middle atmosphere, *Rev. Geophys.*, *41*(1), 1003, doi:10.1029/2001RG000106.

Fritts, D. C., and R. A. Vincent (1987), Mesospheric momentum flux studies at Adelaid, Australia: Observations and a gravity wave/tidal interaction model, *J. Atmos. Sci.*, *44*, 605–619.

Fritts, D. C., and L. Yuan (1989), An analysis of gravity wave ducting in the atmosphere: Eckarts resonances in thermal and Doppler ducts, *J. Geophys. Res.*, *94*, 18,455–18,466, doi:10.1029/JD094iD15p18455.

Fritts, D. C., L. Wang, J. Werne, T. Lund, and K. Wan (2009a), Gravity wave instability dynamics at high Reynolds numbers, 1: Wave field evolution at large amplitudes and high frequencies, *J. Atmos. Sci.*, *66*, 1126–1148, doi:10.1175/2008JAS2726.1.

Fritts, D. C., L. Wang, J. Werne, T. Lund, and K. Wan (2009b), Gravity wave instability dynamics at high Reynolds numbers. 2: Turbulence evolution, structure, and anisotropy, *J. Atmos. Sci.*, *66*, 1149–1171, doi:10.1175/2008JAS2727.1.

Fritts, D. C., D. Janches, and W. K. Hocking (2010), Southern Argentina Agile Meteor Radar: Initial assessment of gravity wave momentum fluxes, *J. Geophys. Res.*, *115*, D19123, doi:10.1029/2010JD013891.

Fritts, D. C., K. Wan, P. Franke, and T. Lund (2012), Computation of clear-air radar backscatter from numerical simulations of turbulence. 3. Off-zenith measurements and biases throughout the lifecycle of a Kelvin-Helmholtz instability, *J. Geophys. Res.*, *117*, D17101, doi:10.1029/2011JD017179.

Fritts, D. C., L. Wang, and J. Werne (2013), Gravity wave-fine structure interactions. Part 1: Influences of fine-structure form and orientation on flow evolution and instability, *J. Atmos. Sci.*, *70*(12), 3710–3734.

Garcia, R. R., and S. Solomon (1985), The effect of breaking gravity waves on the dynamics and chemical composition of the mesosphere and lower thermosphere, *J. Geophys. Res.*, *90*, 3850–3868, doi:10.1029/JD090iD02p03850.

Gavrilov, N. M., S. Fukao, and T. Nakamura (2000), Average statistical characteristics of long gravity waves observed with the middle and upper atmosphere radar in the mesosphere, *J. Geophys. Res.*, *105*(D7), 9365–9379, doi:10.1029/1999JD901092.

Hecht, J. H., R. L. Walterscheid, D. C. Fritts, J. R. Isler, D. C. Senft, C. S. Gardner, and S. J. Franke (1997), Wave breaking signatures in OH airglow and sodium densities and temperatures. 1. Airglow imaging, Na lidar, and MF radar observations, *J. Geophys. Res.*, *102*(D6), 6655–6668, doi:10.1029/96JD02619.

Hecht, J. H., R. L. Walterscheid, M. P. Hickey, and S. J. Franke (2001), Climatology and modeling of quasi-monochromatic atmospheric gravity waves observed over Urbana Illinois, *J. Geophys. Res.*, *106*(D6), 5181–5195, doi:10.1029/2000JD900722.

Hitchman, M. H., K. W. Bywaters, D. C. Fritts, L. Coy, E. Kudeki, and F. Surucu (1992), Mean winds and momentum fluxes over Jicamarca, Peru, during June and August 1987, *J. Atmos. Sci.*, *49*, 2372–2383.
Holton, J. R. (1982), The role of gravity wave induced grad and diffusion in the momentum budget of the mesosphere, *J. Atmos. Sci.*, *39*, 791–799.
Hu, X., A. Z. Liu, C. S. Gardner, and G. R. Swenson (2002), Characteristics of quasi-monochromatic gravity waves observed with Na lidar in the mesopause region at Starfire Optical Range, NM, *Geophys. Res. Lett.*, *29*(24), 2169, doi:10.1029/2002GL014975.
Isler, J. R., M. J. Taylor, and D. C. Fritts (1997), Observational evidence of wave ducting and evanescence in the mesosphere, *J. Geophys. Res.*, *102*(D22), 26,301–26,313, doi:10.1029/97JD01783.
Laughman, B., D. C. Fritts, and J. Werne (2009), Numerical simulation of bore generation and morphology in thermal and Doppler ducts, *Ann. Geophys.*, *27*, 511–523, doi:10.5194/angeo-27-511-2009.
Laughman, B., D. C. Fritts, and J. Werne (2011), Comparisons of predicted bore evolutions by the Benjamin-Davis-Ono and Navier–Stokes equations for idealized mesopause thermal ducts, *J. Geophys. Res.*, *116*, D02120, doi:10.1029/2010JD014409.
Li, Q., J. Xu, J. Yue, W. Yuan, and X. Liu (2011), Statistical characteristics of gravity wave activities observed by an OH airglow imager at Xinglong, in northern China, *Ann. Geophys.*, *29*, 1401–1410, doi:10.5194/angeo-29-1401-2011.
Li, Q., J. Xu, J. Yue, X. Liu, W. Yuan, B. Ning, S. Guan, and J. P. Younger (2013), Investigation of a mesospheric bore event over northern China, *Ann. Geophys.*, *31*, 409–418, doi:10.5194/angeo-31-409-2013.
Li, T., C. Y. She, B. P. Williams, T. Yuan, R. L. Collins, L. M. Kieffaber, and A. W. Peterson (2005), Concurrent OH imager and sodium temperature/wind lidar observation of localized ripples over northern Colorado, *J. Geophys. Res.*, *110*, D13110, doi:10.1029/2004JD004885.
Li, T., C. Y. She, H. L. Liu, and M. T. Montgomery (2007), Evidence of a gravity wave breaking event over Fort Collins, CO (41°N, 105°W), *Geophys. Res. Lett.*, *34*, L05815, doi:10.1029/2006GL028988.
Lombard, P. N., and J. J. Riley (1996), Instability and breakdown of internal gravity waves. I. Linear stability analysis, *Phys. Fluids*, *8*, 3271–3287.
Medeiros, A. F., M. J. Taylor, H. Takahashi, P. P. Batsista, and D. Gobbi (2001), An unusual airglow wave event observed at Cachoeira Paulista 23°S, *Adv. Space Res.*, *27*, 1749–1754.
Medeiros, A. F., J. Fechine, R. A. Buriti, H. Takahashi, C. M. Wrasse, and D. Gobbi (2005), Response of OH, O_2, and OI 5577 airglow emissions to the mesospheric bore in the equatorial region of Brazil, *Adv. Space Res.*, *35*, 1971–1975.
Melo, S. M., R. P. Lowe, W. R. Pendleton Jr., M. J. Taylor, B. Williams, and C. Y. She (2001), Effects of a large mesospheric temperature enhancement on the hydroxyl rotational temperature as observed from the ground, *J. Geophys. Res.*, *106*(A12), 30,381–30,388.
Meyer, W., R. Siebenmorgen, and H.-U. Widdel (1989), Estimates of gravity wave momentum fluxes in the winter and summer high mesosphere over northern Scandinavia, *J. Atmos. Sol. Terr. Phys.*, *51*, 311–319.
Murphy, D. J., and R. A. Vincent (1993), Estimates of momentum flux in the mesosphere and lower thermosphere over Adelaide, Australia, from March 1985 to February 1986, *J. Geophys. Res.*, *98*(D10), 18,617–18,638, doi:10.1029/93JD01861.
Nakamura, T., T. Tsuda, M. Yamamoto, S. Fukao, and S. Kato (1993), Characteristics of gravity waves in the mesosphere observed with the middle and upper atmosphere radar. 1. Momentum flux, *J. Geophys. Res.*, *98*(D5), 8899–8910, doi:10.1029/92JD02978.
Nakamura, T., A. Higashikawa, T. Tsuda, and Y. Matsushita (1999), Seasonal variations of gravity wave structures in OH airglow with a CCD imager at Shigaraki, *Earth Planets Space*, *51*, 897–906.
Nappo, C. J. (2013), *An Introduction to Atmospheric Gravity Waves*, *Int. Geophys. Ser.*, vol. 102, Academic Press, Amsterdam.
Narayanan, V. L., S. Gurubaran, and K. Emperumal (2009), A case study of a mesospheric bore event observed with an all-sky airglow imager at Tirunelveli (8.7°N), *J. Geophys. Res.*, *114*, D08114, doi:10.1029/2008JD010602.
Nielsen, K., M. J. Taylor, R. G. Stockwell, and M. J. Jarvis (2006), An unusual mesospheric bore event observed at high latitudes over Antarctica, *Geophys. Res. Lett.*, *33*, L07803, doi:10.1029/2005GL025649.
Papen, G. C., W. M. Pfenniger, and D. M. Simonich (1995), Sensitivity analysis of Na narrowband wind-temperature lidar systems, *Appl. Optics*, *34*(3), 480–498.
Reid, I. M., and R. A. Vincent (1987), Measurements of mesospheric gravity wave momentum fluxes and mean flow accelerations at Adelaide, Australia, *J. Atmos. Sol. Terr. Phys.*, *49*, 443–460.
Reid, I. M., R. Ruster, P. Czechowsky, and G. Schmidt (1988), VHF radar measurements of momentum flux in the summer polar mesosphere over Andenes (69°N, 16°E), Norway, *Geophys. Res. Lett.*, *15*, 1263–1266, doi:10.1029/GL015i011p01263.
She, C. Y., and R. P. Lowe (1998), Seasonal temperature variations in the mesopause region at mid-latitude: Comparison of lidar and hydroxyl rotational temperatures using WINDII/UARS OH height profiles, *J. Atmos. Sol. Terr. Phys.*, *60*, 1573–1583.
She, C. Y., and J. R. Yu (1994), Simultaneous three-frequency Na lidar measurements of radial wind and temperature in the mesopause region, *Geophys. Res. Lett*, *21*, 1771–1774, doi:10.1029/94GL01417.
She, C. Y., and J. R. Yu (1995), Doppler-free saturation fluorescence spectroscopy of Na Atoms for atmospheric applications, *Appl. Optics*, *34*(6), 1063–1075.
She, C. Y., J. D. Vance, B. P. Williams, D. A. Krueger, H. Moosmuller, D. Gibson-Wilde, and D. Fritts (2002), Lidar studies of atmospheric dynamics near polar mesopause, *Eos Trans. AGU*, *83*(27), 289–300, doi:10.1029/2002EO000206.
She, C. Y., T. Li, B. P. Williams, T. Yuan, and R. H. Picard (2004), Concurrent OH imager and sodium temperature/wind lidar observation of a mesopause region undular bore event over Fort Collins/Platteville, CO, *J. Geophys. Res.*, *109*, D22107, doi:10.1029/2004JD004742.
Shelton, J. D., C. S. Gardener, and C. F. Sechrist Jr. (1980), Density response of the mesospheric sodium layer to gravity wave perturbations, *Geophys. Res. Lett.*, *7*(12), 1069–1072, doi:10.1029/GL007i012p01069.
Simkhada, D. B., J. B. Snively, M. J. Taylor, and S. J. Franke (2009), Analysis and modeling of ducted and evanescent gravity waves observed in the Hawaiian airglow, *Ann. Geophys.*, *27*, 3213–3224.
Smith, S. M., M. J. Taylor, G. R. Swenson, C.-Y. She, W. Hocking, J. Baumgardner, and M. Mendillo (2003), A multidiagnostic investigation of the mesospheric bore phenomenon, *J. Geophys. Res.*, *108*(A2), 1083, doi:10.1029/2002JA009500.
Smith, S. M., J. Friedman, S. Raizada, C. Tepley, J. Baumgardner, and M. Mendillo (2005), Evidence of mesospheric bore formation from a breaking gravity wave event: Simultaneous imaging and lidar measurements, *J. Atmos. Sol. Terr. Phys.*, *67*, 345–356.
Smith, S. M., J. Scheer, E. R. Reisin, J. Baumgardner, and M. Mendillo (2006), Characterization of exceptionally strong mesospheric wave events using all-sky and zenith airglow observations, *J. Geophys. Res.*, *111*, A09309, doi:10.1029/2005JA011197.
Snively, J. B., and V. P. Pasko (2003), Breaking of thunderstorm-generated gravity waves as a source of short-period ducted waves at mesopause altitudes, *J. Geophys. Res.*, *30*(24), 2254, doi:10.1029/2003GL018436.
Snively, J. B., and V. P. Pasko (2008), Excitation of ducted gravity waves in the lower thermosphere by tropospheric sources, *J. Geophys. Res.*, *113*, A06303, doi:10.1029/2007JA012693.
Snively, J. B., V. P. Pasko, and M. J. Taylor (2009), OH and OI airglow layer modulation by ducted short-period gravity waves: Effects of trapping altitude, *J. Geophys. Res.*, *115*, A11311, doi:10.1029/2009JA015236.

Snively, J. B., K. Nielsen, M. P. Hickey, C. J. Heale, M. J. Taylor, and T. Moffat-Griffin (2013), Numerical and statistical evidence for long-range ducted gravity wave propagation over Halley, Antarctica, *Geophys. Res. Lett.*, *40*, 1–5, doi:10.1002/grl.50926.

Sonmor, L. J., and G. P. Klaassen (1997), Toward a unified theory of gravity wave stability, *J. Atmos. Sci.*, *54*, 2655–2680.

Stockwell, R. G., M. J. Taylor, K. Nielson, and M. J. Jarvis (2006), A novel joint space-wave number analysis of an unusual Antarctic gravity wave event, *Geophys. Res. Lett.*, *33*, L08805, doi:10.1029/2005GL025660.

Stockwell, R. G., M. J. Taylor, K. Nielson, and M. J. Jarvis (2011), The evolution of a breaking mesospheric bore wave packet, *J. Geophys. Res.*, *116*, D19102, doi:10.1029/2010JD015321.

Strobel, D. F., J. P. Apruzese, and M. R. Schoeberl (1985), Energy balance constraints on gravity wave induced eddy diffusion in the mesosphere and lower thermosphere, *J. Geophys. Res.*, *90*, 13,067–13,072, doi:10.1029/JD090iD07p13067.

Suzuki, S., K. Shiokawa, Y. Otsuka, T. Ogawa, M. Kubota, M. Tsutsumi, T. Nakamura, and D. C. Fritts (2007), Gravity wave momentum flux in the upper mesosphere derived from OH airglow imaging measurements, *Earth Planets Space*, *59*, 421–428.

Swenson, G. R., and C. S. Gardener (1998), Analytical models for the responses of the mesospheric OH* and Na layers to atmospheric gravity waves, *J. Geophys. Res.*, *103*(D6), 6271–6294, doi:10.1029/97JD02985.

Swenson, G. R., and S. B. Mende (1994), OH emission and gravity waves (including a breaking wave) in all-sky imagery from Bear Lake, UT, *Geophys. Res. Lett.*, *21*(20), 2239–2242, doi:10.1029/94GL02112.

Swenson, G. R., M. J. Taylor, P. J. Espy, C. Gardner, and X. Tac (1995), ALOHA-93 measurements of intrinsic AGW characteristics using airborne airglow imager and ground-based Na wind/temperature lidar, *Geophys. Res. Lett.*, *22*(20), 2841–2844, doi:10.1029/95GL02579.

Swenson, G. R., R. Haque, W. Yang, and C. S. Gardener (1999), Momentum and energy fluxes of monochromatic gravity waves observed by an OH imager at Starfire Optical Range, New Mexico, *J. Geophys. Res.*, *104*, 6067–6080, doi:10.1029/1998JD200080.

Taylor, M. J., and M. A. Hapgood (1988), Identification of a thunderstorm as a source of short period gravity waves in the upper atmospheric nightglow emissions, *Planet. Space Sci.*, *36*, 975–985.

Taylor, M. J., E. H. Ryan, T. F. Tuan, and R. Edwards (1993), Evidence of preferential directions for gravity wave propagation due to wind filtering in the middle atmosphere, *J. Geophys. Res.*, *98*(A4), 6047–6057, doi:10.1029/92JA02604.

Taylor, M. J., M. B. Bishop, and V. Taylor (1995a), All-sky measurements of short period waves imaged in the OI(557.7 nm), Na(559.2 nm) and near infrared OH and O_2(0,1) nightglow emissions during the ALOHA-93 Campaign, *Geophys. Res. Lett.*, *22*(20), 2833–2836, doi:10.1029/95GL02946.

Taylor, M. J., D. N. Turnbull, and R. P. Lowe (1995b), Spectrometric and imaging measurements of a spectacular gravity wave event observed during the ALOHA-93 Campaign, *Geophys. Res. Lett.*, *22*(20), 2849–2852, doi:10.1029/95GL02948.

Taylor, M. J., W. R. Pendleton, S. Clark, H. Takahashi, D. Gobbi, and R. A. Goldberg (1997), Image measurements of short-period gravity waves at equatorial latitudes, *J. Geophys. Res.*, *102*(D22), 26,283–26,299, doi:10.1029/96JD03515.

Tsuda, T., Y. Murayama, M. Yamamoto, S. Kato, and S. Fukao (1990), Seasonal variation of momentum flux in the mesosphere observed with MU radar, *Geophys. Res. Lett.*, *17*, 725–728, doi:10.1029/GL017i006p00725.

Vadas, S. L., and M. J. Nicolls (2009), Temporal evolution of neutral, thermospheric winds and plasma response using PFISR measurements of gravity waves, *J. Atmos. Sol. Terr. Phys.*, *71*, 744–770.

Vincent, R. A., and I. M. Reid (1983), HF Doppler measurements of mesospheric momentum fluxes, *J. Atmos. Sci.*, *40*, 1321–1333.

von Zahn, U., K. H. Fricke, R. Gerndt, and T. Blix (1987), Mesospheric temperatures and OH layer height as derived from ground-based lidar and OH* spectrometry, *J. Atmos. and Terr. Phys.*, *49*, 863–868, doi:10.1016/0021-9169(87)90025-0.

Walterscheid, R. L., and M. P. Hickey (2009), Gravity wave ducting in the upper mesosphere and lower thermosphere duct system, *J. Geophys. Res.*, *114*, D19109, doi:10.1029/2008JD011269.

Walterscheid, R. L., J. H. Hecht, R. A. Vincent, I. M. Reid, J. Woithe, and M. P. Hickey (1999), Analysis and interpretation of airglow and radar observations of quasi-monochromatic gravity waves in the upper mesosphere and lower thermosphere over Adelaide, Australia (35°S, 138°E), *J. Atmos. Sol. Terr. Phys.*, *61*(6), 461–478.

Wang, D.-Y., and D. C. Fritts (1990), Mesospheric momentum fluxes observed by the MST Radar at Poker Flat, Alaska, *J. Atmos. Sci.*, *47*, 1511–1521.

Williams, B. P., D. C. Fritts, C. Y. She, and R. A. Goldberg (2006), Gravity wave propagation through a large semidiurnal tide and instabilities in the mesosphere and lower thermosphere during the winter 2003 MaCWAVE rocket campaign, *Ann. Geophys.*, *24*, 1199–1208, doi:10.5194/angeo-24-1199-2006.

Xu, J., A. K. Smith, R. L. Collins, and C.-Y. She (2006), Signature of an overturning gravity wave in the mesospheric sodium layer: Comparison of a nonlinear photochemical-dynamical model and lidar observations, *J. Geophys. Res.*, *111*, D17301, doi:10.1029/2005JD006749.

Yamada, Y., H. Fukunishi, T. Nakamura, and T. Tsuda (2001), Breaking down of small-scale quasi-stationary gravity wave and transition to turbulence observed in OH airglow, *Geophys. Res. Lett.*, *28*, 2153–2156, doi:10.1029/2000GL011945.

Yue, J., S. L. Vadas, C.-Y. She, T. Nakamura, S. C. Reising, H.-L. Liu, P. Stamus, D. A. Krueger, W. Lyons, and T. Li (2009), Concentric gravity waves in the mesosphere generated by deep convective plumes in the lower atmosphere near Fort Collins, Colorado, *J. Geophys. Res.*, *114*, D06104, doi:10.1029/2008JD011244.

Zhao, Y., M. J. Taylor, and X. Chu (2005), Comparison of simultaneous Na lidar and Mesospheric Temperature Mapper measurements and the effects of tides on the emission layer heights, *J. Geophys. Res.*, *110*, D09S07, doi:10.1029/2004JD005115.

Erratum

In the originally published version of this article, there were errors in the symbols for equation 3 and equation 9. The erroneous symbols have since been corrected and this version may be considered the authoritative version of record.